Journal Name

ARTICLE

Inherent Predominance of High Chiral Angle Metallic Carbon Nanotubes in Continuous Fibers Grown From Molten Catalyst

B. Alemán,[a] M. Mar Bernal,[b] B. Mas,[a] Emilio M. Pérez,[b] V. Reguero,[a] G. Xu,[a] Y. Cui,[a] Juan J. Vilatela†[a]

We present evidence that high temperature CVD growth of SWNTs under conditions for continuous spinning of macroscopic fibers leads to an inherent predominance of high chiral angle CNTs, peaking at the armchair end. Raman, UV-vis-NIR absorption, and photoluminescence spectroscopy measurements show prevalence of metallic SWNTs. The complete chiral angle distribution is obtained by electron diffraction of over 390 CNTs. It is biased towards high chiral angles and peaks at the armchair end (30˚), in good agreement with established atomistic models for SWNT growth from liquid catalyst. Based on the Fe-C-S constituent binary and ternary phase diagrams, thermodynamic calculations of phase compositions from fast cooling and experimental evidence of post-synthesis catalyst, the proposed thermodynamic path of the catalyst is to form a solid FCC Fe core and a liquid Fe-S shell. S in the outer liquid shell first stabilizes the edge of the nascent CNT, but once a graphitic wall forms it is rejected due to the high interfacial energy with the Fe-C-S alloy.

Introduction

There is an ever increasing interest in producing macroscopic ensembles of nanocarbons in the forms of membranes, 3D architectures and fibers. In the case of carbon nanotubes (CNTs), their assembly into continuous macroscopic fibers has led to axial properties rivaling or surpassing those of high-performance engineering materials.[1,2,3] These fibers have also emerged as a unique electrode in a variety of hybrid devices for energy harvesting and storage, as well as in other applications,[4,5] giving further momentum to their synthesis on a semi-industrial scale.[6] In addition to their technological relevance, the development of CNT fiber spinning methods has often provided new insight into long standing unresolved issues in the broader field of CNT materials science. Such is the case for the direct spinning process, in which CNTs synthesized by floating catalyst chemical vapor deposition (CVD) associate in the gas phase to form an aerogel that can be continuously drawn out of the reactor and wound as a macroscopic fiber.[7] This CVD reaction has special features compared to "traditional" substrate-based CNT growth by CVD. It requires a hydrogen atmosphere and a small amount of sulfur promoter,

and is carried out at 1100-1350˚C, ~500°C higher than the substrate processes. Under these conditions the nanotubes grow up to the mm scale in seconds (or less) and are predominantly of fewer layers and larger diameter than in conventional processes. [8] Such exceptionally fast growth rate and a combined large-diameter and few-layer morphology are strongly related to the presence of sulfur (S). It limits carbon (C) diffusion into the catalyst particles while also assisting C reconstruction into graphitic segments of nascent CNTs.[8,9] Metallurgy literature suggests this role of S to be similar to that of O,[8] which if added in small amounts can enhance CNT growth in low temperature CVD (often referred to as "super growth") by preventing catalyst blockage.[10] Furthermore, Sundaram et al. showed that continuous fibers of almost exclusively metallic single-walled carbon nanotubes (SWNTs) could be produced using CS_2 and methane as sulfur and carbon precursors, respectively.[11] This was attributed to S lowering the activation energy for Stone-Thrower-Wales dislocation motion involved in the rotation of the graphene layer with the <100> parallel to the tube axis while the nascent CNT increases in diameter.

Fixation of chiral angles during low temperature CVD growth of CNTs has been attributed to: chiral angle effects on energy of CNT edge in nascent tube[12] and on growth rates,[13,14] lifetime selectivity,[15] and defect-directed graphene layer rotations in specific symmetry directions.[16] Overall, there is not a unified view nor full agreement with experiment data on the predominance of specific chiral angles.[17] Typical methods to directly (i.e. without post-growth separation) produce samples rich in specific chiral angles would thus seem to circumvent the intrinsic complexity in "standard" CNT growth. They include

a. IMDEA Materials Institute, c/ Eric Kandel 2, Getafe 28906, Madrid, Spain.
b. IMDEA Nanoscience Institute, c/Faraday 9, Ciudad Universitaria de Cantoblanco, 28049, Madrid, Spain.
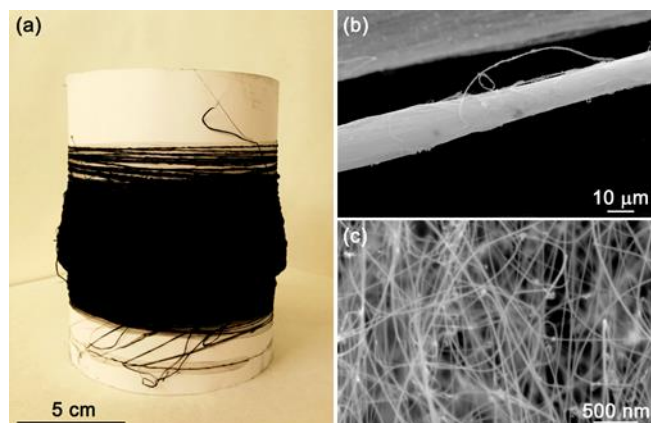† Corresponding author: juanjose.vilatela@imdea.org

Fig. 1. (a) Photograph of a SWNT fiber sample produced after 2 hours of continuous spinning. SEM micrographs of (b) an individual CNT fiber filament and (c) the CNT bundles that make up the fiber.

the pre-formation of CNT segments by surface-catalysed cyclodehydrogenation of molecular precursors, used then as seeds for CVD growth;[18] and the use of a high-melting point bimetallic catalyst that remains crystalline at the point of reaction and favours growth of specific CNTs through matching of the CNT circumference to one of the planes of the solid catalyst.[19]

To contribute to the growing interest in this field, and with the long-term vision of controlling chiral angles in CNT synthesis, here, we present new evidence of continuous CNT fibers with chiral distribution biased towards armchair. By a combination of Raman, ultraviolet-visible-near infrared (UV-Vis-NIR) absorption and photoluminescence excitation (PLE) spectroscopies, we first show the metallic character of the CNTs in such macroscopic fibers. Then we obtain a distribution of chiral angles from selected area electron diffraction (SAED) and show that the chiral angle distribution is close to the one predicted by Yakobson and co-workers for a molten catalyst.[14] We then propose a path of the catalyst particle based on the bulk Fe-S-C constituent binary and ternary phase diagrams, as well as on thermodynamic calculations of phase compositions resulting from fast cooling. A key prediction is that the surface of the catalyst is S rich and remains liquid throughout the growth process. The results are consistent with X-ray diffraction (XRD), SAED and energy dispersive X-ray spectroscopy (EDS) observations of the catalyst having a FCC Fe core and $Fe_{1-x}S$ shell after synthesis. Under all of the conditions we have tested so far, the bias towards high chiral angles is independent from the choice of C source (butanol, toluene) or promoter (thiophene-S, selenophene-Se), provided it leads to growth of SWNTs.

Results and discussion

The samples in this work consist of macroscopic fibers with diameters of 10-20 μm, produced under conditions that enable continuous spinning for hours (Fig. 1a). The type of CNT is adjusted to SWNT by using a low ratio of $S/C = 4.4 \times 10^{-4}$

Fig. 2. CNT fiber Raman spectra acquired with (a) 785 nm, (b) 633 nm and (c) 532 nm lasers showing RBM Raman intensities, with apparent predominance of metallic SWNTs. Approximate chiral angles are indicated.
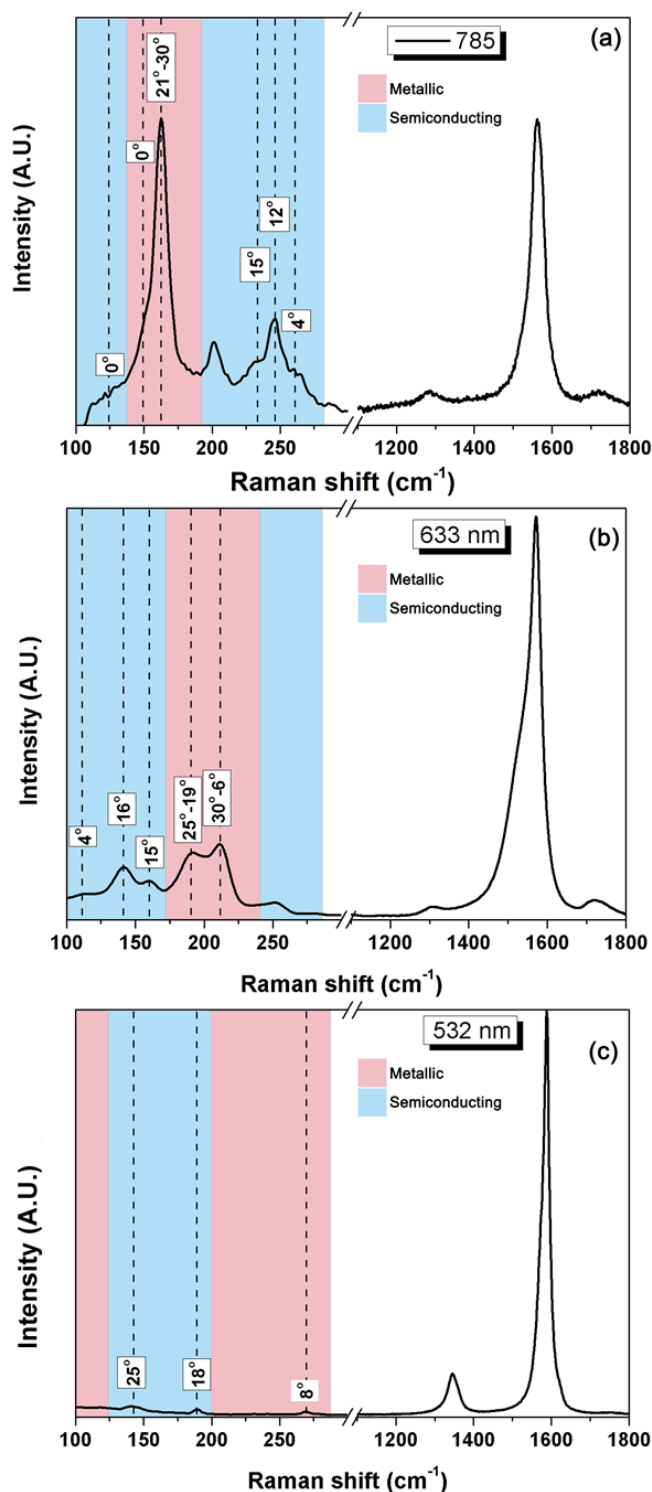
during the reaction.[20] Typical scanning electron microscopy (SEM) micrographs of a filament and the CNT bundles that form it are shown in Fig. 1b,c. An individual fiber is made up of bundles of tens of nm, each comprised of around 20 nanotubes, so that there are roughly 10^7 nanotubes per cross section. The first part of this work analyses the electronic nature of the SWNTs, both in aggregated fiber state and dispersed in quasi-individualized form. The second part presents a distribution of chiral angles and its relation to the catalyst state at the point of reaction.
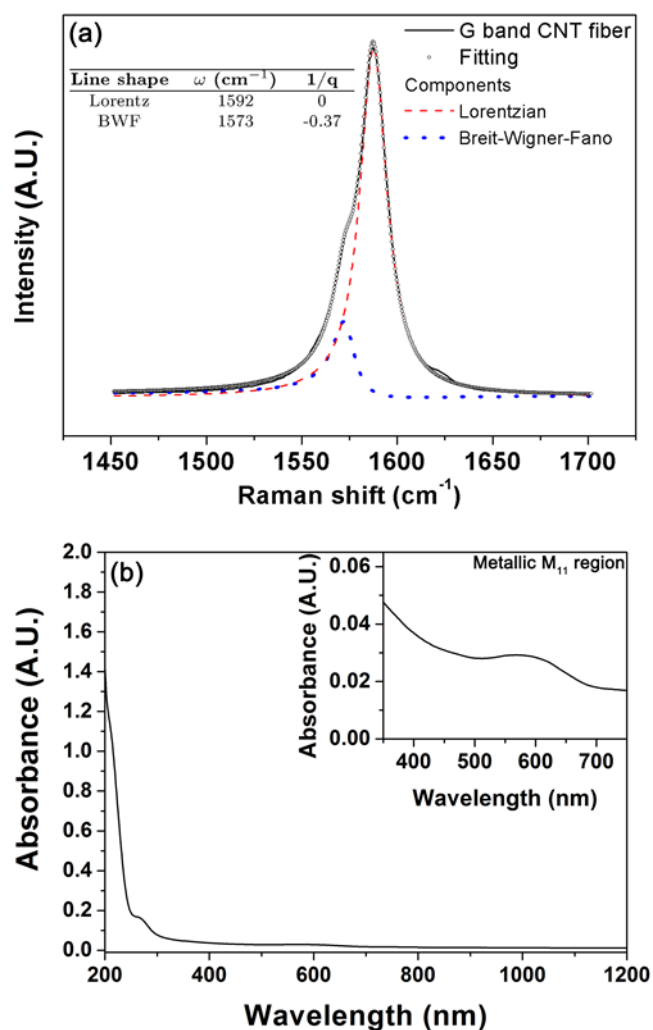
ARTICLE

CNT type from spectroscopy measurements

Fig. 2 shows Raman spectra of CNT fibers for 785 nm, 633 nm and 532 nm laser lines. At first sight, the spectra are indicative of highly graphitic CNTs, with an intensity ratio of the D/G bands < 0.1. The position and shape of the radial breathing modes (RBMs) indicates a predominantly SWNT sample, in accordance with the transmission electron microscopy (TEM) data (see below) and previous results.[20] From the dependence of 1/diameter (d) on optical transition energies between van Hove singularities, assuming a relationship between the diameter and the Raman shift of the RBMs (ω_{RBM}) of d = 248/ ω_{RBM},[21] the observed RBMs correspond to a range of SWNT diameters of 0.9-2.0 nm. The highest RBM intensities relative to the G band are consistently observed for the 785 nm laser line, and particularly in the Raman shift region corresponding to metallic (M) CNTs (see Fig. S1 and ref. [22]). In comparison, with 532 nm excitation, which corresponds mainly to the resonance of semiconducting (SC) CNTs, RBM intensities are substantially lower, suggesting a lower fraction of this type of CNTs. Inspection with 633 nm, which covers both SC and M CNTs, again points to more intense signals from M tubes. Most RBMs are highly resolved, enough to attempt assignation of chiral indices (Fig. S1), but considering the difficulties involved in an unambiguous determination of (n,m),[23] we prefer to stay on safer grounds and consider the Raman evidence of predominance of metallic CNTs in our samples. Moreover, the resonance window linewidth (FWHM ~ 50 meV) probed with a laser is very small compared with the range of CNTs expected in a 1 nm-wide window of CNT diameters, which implies that only a small fraction of the CNTs under the laser spot are observed in resonant Raman measurements (S1).

In agreement with the RBMs observed, the line shape of the G band also reflects the predominance of metallic SWNTs (Fig. 3a). It presents the typical broadening of metallic SWNTs due to a low frequency G band component arising from the coupling of lattice vibrations to free electrons.[24] It can be accurately fitted by the corresponding Breit-Wigner-Fano (BWF) line shape[25], and results in an asymmetric factor 1/q ranging from -0.14 to -0.4, in agreement with the value of around -0.2 reported for M-SWNTs. [26,27]

The interpretation of the Raman spectra can be confidently applied to the whole macroscopic continuous CNT fibers. In addition to taking several spectra along different locations along a fiber sample and on samples from different batches, we note that even for a single measurement the 1 micron laser spot probes more than ~10^4 CNTs on the surface.

To get further spectroscopic evidence, we pre-shortened the CNT fibers down to ~100 μm length using an ion beam, to facilitate their dispersion (S2). Upon ultra sonication and

centrifugation, the samples produced suspensions in 1% SDS solution in D_2O of sufficient quality to obtain their UV-vis-NIR absorption spectrum (Fig. 3b). The absorption feature in the UV region (200-300 nm) is a characteristic feature of SWNTs, related to the plasmon resonances of the free electron cloud of π electrons.[28,29] In the vis-NIR region, the spectrum shows a broad absorption peak centred at ca. 600 nm, characteristic of the first van Hove electronic transitions (M_{11}) of metallic SWNTs.[30,31] No absorption bands for S_{11} and S_{22} transitions in semiconducting SWNTs were found.[32,33] In agreement with the absorption features, no excitation/emission peaks were found in the PLE map (Fig. S3). Although this does not rule out entirely the presence of small amounts of SC tubes, it does indicate that they are in such small proportion relative to metallic SWNTs that their PL quantum yield is below the resolution of our equipment. The fact that some SC CNTs can be observed by Raman (Fig. 2) but not PLE is due to their strong resonance under laser excitation and high intensities of the anti-Stokes Raman signal from a fiber, compared with emission from a small number of CNTs in dispersion. The combined evidence of Raman, UV-vis-NIR and PLE spectroscopies is conclusive with regards to the prevalence of metallic SWNTs in the CNT fibers.

In addition to a metallic character, most RBMs detected by Raman correspond to large chiral angles. In Fig. 2a we have included approximate values of chiral angles for the different

Fig. 3. (a) G band region of Raman spectra for CNT fiber showing the metallic line shape of the CNT fiber with a BWF asymmetric parameter 1/q of -0.37. (b) UV-vis-NIR spectrum of a dispersion of the fiber constituent CNTs in D_2O solution with 1 wt. -% sodium dodecyl sulfate (SDS). The absorption spectrum shows the first-order transition from M SWNTs M_{11} (inset), but no absorption peaks from SC SWNTs.

RBM regions probed by Raman. While the high chiral angle dominance is expected for armchair tubes ($n=m$ and $\chi = 30°$), there is a wide range of semi-metallic tubes for which this would not necessarily be the case. Thus, the data in Fig. 2 would suggest both metallic predominance and a bias towards high chiral angles, which are equivalent in the case of armchair and quasi-metallic CNTs of type ($n, n-3$), for example. In this respect, however, conventional Raman spectroscopy without a tunable laser is alone not well suited to look for specific chiral angle predominance in a large ensemble of CNTs. We therefore use electron diffraction in TEM as a direct technique to determine the chiral angles of SWNTs within bundles.[34]
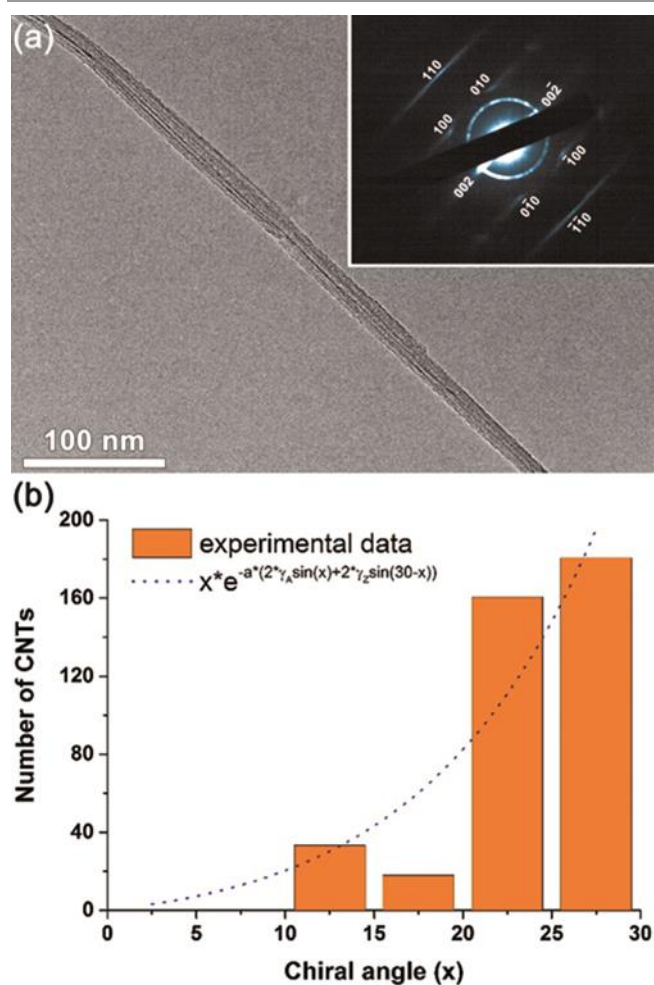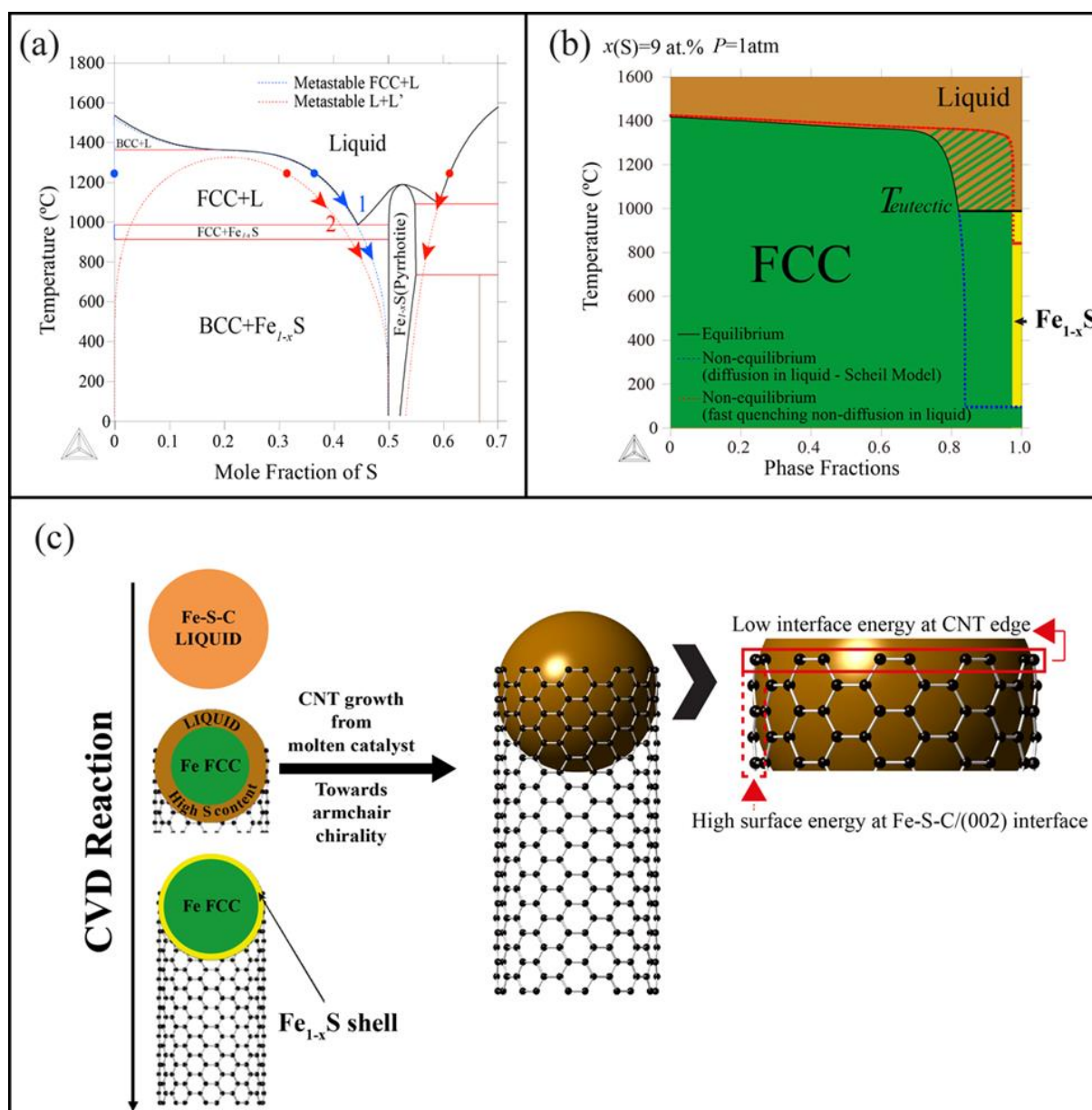

Fig. 4. Chiral angles of SWNTs extracted from TEM measurements. (a) SWNT bundle and its corresponding SAED pattern presenting the characteristic armchair diffraction pattern. (b) Chiral angle distribution obtained from SAED patterns showing that 80% of the CNT bundles analyzed present chiral angle in the range of 20°-30°. For reference, the dashed line shows the distribution lineshape of theoretical predictions for molten catalysts after Yakobson and co-workers.[14]

metallic). Overall, we have successfully extracted chiral angles from SAED patterns of over 20 bundles (S4). Counting the number of CNTs in each bundle then, gives us a distribution of chiral angle for over 390 CNTs, which we present in Fig. 4b. By performing SAED on bundles rather than individual CNTs, we have increased the number of CNTs analyzed and therefore the statistical significance of the plot, but at the expense of introducing CNT misalignment within a bundle as a possible source of error of around ±4°. The distribution in Fig. 4b shows a clear bias towards high chiral angles, with abundance increasing past the 19.1˚ "magic angle" of ($2m,m$) tubes[35] and peaking at the armchair end. Interestingly, there is complete absence of zig-zag CNTs or with chiral angles below 10˚. Before discussing some implications of the high chiral angle predominance, we note that our observations of fibers produced under different synthesis conditions suggest that the distribution in Fig. 4b is not unique, but intrinsic to the SWNT growth in the direct fiber spinning process. TEM observation of CNT fibers produced from a different C precursor (toluene instead of butanol) or using a different promoter (Se instead of S)[36] also give high CNT chiral angles (S5). The observation that the high-chiral angle predominance is apparently independent of the choice of C precursor amongst butanol and toluene is also important because it rules out the possibility of the distribution arising from O from the precursor selectively etching low chiral angle CNTs. This is also in line with the observation of nearly all-armchair CNT fibers produced by Sundaram et al. from CS_2 and methane[11], also an O-free precursor mixture.

Although not without exceptions,[37] the model of Yakobson has proven effective in predicting chiral angle distributions observed in several samples of CNTs grown by CVD[13] without recalling specific catalyst states or epitaxial relations, and would thus seem suitable to describe our results. In such model, abundance of CNTs is seen as the product of nucleation and growth rates. Both depend on CNT diameter and chiral angle, the growth according to a screw dislocation mechanism,[13] and nucleation dictated by the perimeter of the nascent CNT in contact with the catalyst.[12] For solid catalyst, growth penalizes achiral CNTs and nucleation penalizes chiral CNTs, leading to a narrow abundance distribution peaking at near-armchair CNTs. When the catalyst is in liquid state and can therefore adapt to the CNT perimeter, there is no penalty in achiral CNTs (e.g. armchair) and growth rate is proportional to chiral angle (χ), producing a slightly broader distribution that includes more low chiral angles but which extends to the armchair side where it peaks. In Fig. 4b we include for reference a curve fit following the theoretical predictions for molten catalyst according to this model. This analytical expression is not a best fit, but there is overall agreement in the trend and the fitting confirms the predominance of high

SWNTs bundle chirality from electron diffraction

Fig. 4a shows a typical SAED of a bundle of 10 nanotubes. The strong {110} type reflections perpendicular to the (002), and chiral angle of 30°, corresponding to an armchair nanotube (i.e.

Fig. 5. Thermodynamic analysis of the Fe-S-C catalyst phase composition during CNT growth. (a) Fe-S equilibrium phase diagram and calculation of fast cooling processes superimposed. Blue line: Scheil model with suspended eutectic transformation (lower limit). Red line: Sheil model and a possible second liquid phase richer in S (upper limit). (b) Phase fraction evolution showing the presence of a liquid shell down to at least 1000°C. (c) Schematic showing the growth of the CNT from an FCC core-FeS shell catalyst particle. S lowers the interface energy at the CNT edge and favours its nucleation, but the interface of Fe-S-C and the basal plane of graphite is non-wetting, leading to the ejection of the graphitic layer (i.e. extrusion of the CNT).

chiral angles through the lower edge energy of armchair ($\gamma_A \approx 0$) compared with zig-zag ($\gamma_Z \approx 0.45$ eV/Å), with γ_Z being of the order expected ($\gamma_Z \approx 1.45$ eV/Å). Though γ_A is lower than expected, and the exponent constant, $a = \pi d/k_B T$, a factor of 50 higher than in the model, the agreement is surprisingly good, especially considering that the chemical potential of the catalyst-C at the nascent CNT edge[12] has not been taken into account. An important implication of this agreement is the suggestion that the catalyst is in molten state, something that is suspected for our high temperature CVD but which is difficult to fully prove.

Molten catalyst and thermodynamic analysis

Although the catalyst phase has not been determined at the point of reaction, we present experimental post-synthesis evidence and thermodynamic calculations to show that it should indeed be in liquid state.

The catalyst particle size alone, in the range of 2 nm would lower substantially its melting point on account of the well-known Gibbs-Thomson effect, to about 1050°C for pure Fe.[38,39] Sulfur and carbon further stabilize the liquid, with eutectics about 400°C lower for the bulk binary systems compared to elemental Fe. Yet, more compelling evidence of the state of the catalyst can be obtained by examination of catalyst particles post-synthesis, from which we extract an approximate elemental composition that then allows for a prediction of phases at 1250°C and throughout rapid cooling.

From EDS measurements we estimate an atomic ratio of S/Fe of 0.090 +/- 0.004, or a mass fraction around 5wt. % (S6). Furthermore, we know from XRD and HRTEM that FCC Fe

predominates, that there is no BCC Fe, only a very small amount of cementite (CM) (only observed in a small fraction of very large inactive particles) and no presence of FeO_x (S6). S is only detected by EDS and X-ray Photoelectron Spectroscopy (XPS), and is present as a Fe-S intermetallic (S6). This intermetallic can be expected to be at the surface, based on reports for bulk metallurgical samples of Fe-C-S melts in contact with graphite, where S is always found on the surface,[40] and on STEM observations on similar CNT samples.[8] At such concentration at the surface of a ∼2nm particle, the intermetallic corresponds to a subnanometric layer, which explains why it cannot be observed by diffraction techniques (S6). The resulting (post-synthesis) catalyst particle is most likely a Fe-S shell, and a much larger FCC Fe core with a small amount of C and probably little, if any S. Nevertheless, the bulk characterisation methods used (XPS, XRD, EDS) probe both active and inactive particles, and thus more conclusive evidence of this core-shell catalyst structure requires direct observation of the catalyst in the SWNTs. However, because of the challenge in finding the ∼1nm particle inside an individual ∼1mm long-CNT and carrying out spatially-resolved EDS on it, this confirmation remains pending. Before presenting our own thermodynamic calculations on the catalyst alloy particle, it is instructive to consider the constituent binary and ternary equilibrium phase diagrams in relation to the expected formation of individual phases during cooling, even as a qualitative description that for now ignores interfacial energies or size effects (see Fe-S diagram in Fig. 5a and isothermal sections of ternary in S7). The composition of the particle is Fe-rich, well below the Fe-C and Fe-S eutectics, and possibly also below the C-rich liquid and S-rich liquid of the ternary system, but most likely of sufficient concentrations of S and C to ensure that the particle is in metastable molten state at 1250 °C. Cooling from the molten state, the first expected phase transformation is the creation of a stable FCC nucleus, upon which S is rejected to the surrounding liquid owing to the negligible solubility of S in FCC (< 0.1 at.%). As the FCC core grows, liquid is increasingly enriched with S until an intermetallic $Fe_{1-x}S$ (pyrrhotite) forms. Although the exact composition of the liquid is unknown (between a single liquid or a mixture of C-rich and S-rich liquids, L, L_1, L_2, respectively), the Fe-C-S ternary diagram does show that the S-rich liquid is more stable and therefore predominates. Due to the lack of a full set of thermodynamic data (note that a full thermodynamic assessment of the ternary system requires a set of consistent parameters to represent both thermochemistry properties and phase diagram data) for the ternary system, we focus for now on the Fe-S system as representative of the liquid covering the FCC Fe core and later on the core-shell structure.

The core-shell path could be confirmed by thermodynamic calculations of phase fraction of solid phases during fast cooling (quenching). In view that the catalyst is rich in S at the corner of the ternary diagram, we have made the calculation of Fe-9at.%S binary melts using ThermoCalc Software. Fig. 5a shows the thermodynamic path of the liquid around the FCC Fe nuclei along the liquidus line highlighted on the Fe-S binary diagram, whereas Fig. 5b displays the corresponding phase fraction (solid line). The equilibrium process (solid line) predicts more than

15% fraction of liquid even at temperatures as low as 1000˚C, which then undergoes the eutectic transformation. In our CVD process, however, the cooling rate of the catalyst particle is as high as 150°C/s (S7). In Fig. 5b we present lower (dashed blue line) and upper (dashed red line) limits for the phase fraction evolution of the catalyst during fast cooling. To account for the effect of undercooling during fast cooling, the dashed lines are calculated by suspending/retarding the formation of FCC/$Fe_{1-x}S$(pyrrhotite) eutectics, yet preserving primary FCC. The lower limit (in blue) is obtained by using the conventional Scheil model which assumes no back diffusion in solid, but diffusion so fast in liquid that the uniform composition distribution can be achieved instantly.[41] Because the solubility of sulphur in FCC is negligible, the predicted solid fraction using the conventional Scheil model and in equilibrium condition are similar. The lower bound in the phase diagram is thus simply the extension of the liquidus line down to a divorced eutectic (i.e. a eutectic without lamella structure even in the bulk). The upper limit of the phase fraction (in red) not only considers the conditions of Scheil model but also allows for the possibility of a phase transformation into a second liquid richer in S (L') upon fast cooling. The higher S content in L' would increase the phase fraction of primary FCC phase but still with a liquid shell surrounding it. The two boundaries confirm, as expected, that the outer layer of the catalyst particle in our CVD process is in liquid state at the temperatures relevant for CNT growth, leading to the formation of a core (Fe)–shell ($Fe_{1-x}S$) structure though a phase transformation pathway in between the two cases calculated.

All the evidence above strongly supports the view of a core-shell catalyst. Its evolution, coupled to the most plausible stages of CNT growth, is schematically shown in Fig. 5c. The formation of S-rich liquid at the surface limits C diffusion of C into the "bulk" of the particle compared to a S-free system. There, it acts as a promoter in the catalytic decomposition of the incoming C-containing molecules from the gas-phase, very much in line with its role in methanation on transition metal catalysts, where in small quantities S prevents sub-surface C diffusion but leads to the formation of layered graphitic deposits.[42] The formation of transient C-S bonds would stabilize the edge of a nascent CNT and lower the interfacial energy between the graphite lattice *edge* and the Fe-S-C molten catalyst. However, once a graphitic ring or hemisphere is formed around the particle, an interfacial *area* between the graphite lattice basal plane and the catalyst is formed. Its corresponding interfacial energy in fact carries a large energy penalty. Molten Fe-S-C is known not to wet graphite, even at small S concentrations <1at. % S.[40] This rejection of graphitic carbon probably plays an important role in the exceptionally fast extrusion of the CNTs in the direct spinning process, of the order of mm/s.

The simple model discussed above has currently various limitations, most evidently ignoring the fact that the particles are essentially clusters of around 500 atoms. Yet, its value is in establishing a link between the thermodynamics of the phase composition in the bulk Fe-S-C system upon rapid cooling, and a well-established atomistic model for CNT growth. It shows agreement in the role of sulfur: i) constraining C diffusion to the

surface ii) stabilising the edge of a nascent CNTs, and iii) promoting graphite edge growth. The resulting chiral angle distributions for SWNTs are thus close to those predicted by atomistic models for molten catalyst, in which chiral angles are imposed at the nucleation stage. The fact that we observe predominance of armchair CNTs irrespective of C source, or using Se as promoter (with similar thermodynamics of phase compositions) further supports the view that this is an inherent feature of high temperature CVD growth of SWNTs and therefore of the direct CNT fiber spinning process.

Experimental

CNT fibers were synthesized by the direct spinning of CNTs from the gas phase during growth by floating catalyst CVD,[7] using butanol as carbon source, ferrocene as iron catalyst and thiophene as a sulfur catalyst promoter.[20] The reaction was carried out in hydrogen atmosphere at 1250°C. The samples analyzed included fiber from different batches to ensure reproducibility of the CVD reaction conditions. Selected samples were produced using Se as promoter,[36] or toluene as the C source.

SEM and ion milling were carried out with an FIB-FEGSEM Helios NanoLab 600i (FEI) at 30 kV. TEM was performed with a JEOL JEM 3000F TEM at 300 kV while selected area electron diffraction patterns were obtained at 200 kV with a JEOL JEM 2000FX. Catalyst structure was determined from the Fast-Fourier-Transform of lattice-resolved micrographs. EDS was performed with an EVO MA15 SEM operated at 15kV and a JEOL JEM 2800 in STEM mode at 200kV.

Raman spectroscopy was performed mainly using a Bruker Senterra equipped with laser lines of 532, 633 and 758 nm. Additional measurements were carried out with a using a Jasco NRS-5100, using laser lines of 532 nm and 785 nm, and a Renishaw micro-spectroscopy system with a 532nm laser. A least ten separate measurements in different areas of the fibers were collected for each laser line.

Optical absorption data were recorded from 200 to 1600 nm with a UV-vis-NIR spectrophotometer (Agilent Cary 5000), using a quartz cell with a path length of 1 cm. Pre-shortened CNT fibers were dispersed in D_2O, 1 % sodium dodecyl sulfate (SDS), 298 K. The spectral resolution was 1 nm.

PLE intensity maps were obtained with a HORIBA Nanolog 4 equipped with a liquid-nitrogen cooled InGaAs near-IR array detector. The excitation wavelength was varied from 500 to 800 nm in 5-nm steps and the emission wavelength was varied from 800 to 1550 nm in 5-nm steps.

XRD measurements were performed at the Non-crystalline Diffraction beam line at Alba Light Source using a wavelength of 1Å. 2D wide-angle X-ray scattering patterns were azimuthally integrated to obtain radial profiles. The data shown are after sample-detector distance calibration.

CALPHAD (CALculation of PHAse Diagram) type computational thermodynamics is used in this work for representing Fe-S phase diagram. It consistently evaluates and represents both thermochemistry properties and phase diagrams via a set of self-consistent parameters based on the Compound Energy Formulism (CEF) model. The parameters are optimized via weighted a least-square algorithm implemented by ThermoCalc Software. In this work, we adopted the latest Fe-S thermodynamic database by Dilner et al.[43] in our calculations. The prediction of phase fraction during the fast cooling was obtained using the Scheil model, where the solid phases were assumed 'frozen', and thus the simulated solidification path was allowed to reach the eutectic path in the Fe-S binary.

XPS data were collected in a SPECS GmbH electron spectroscopy system provided with a PHOIBOS 150 9MCD analyzer.

Conclusions

Our results show that continuous fibers of SWNTs directly spun from the gas phase during high temperature CVD growth present an inherent predominance of metallic and high chiral angle CNTs. The metallic character is manifested by the broadening of the Raman G band, with a Breit-Wigner-Fano lineshape with an asymmetric factor q ranging from -0.14 to -0.4, in agreement with M-SWNTs values. On the other hand, U-Vis-NIR absorption spectrum shows the first order transition van Hove electronic transitions M_{11} centered at 600 nm and no detectable absorption peaks from semiconducting CNTs. No PLE from semiconducting tubes is observed either.

Chiral angles for SWNT bundles measured by electron diffraction in TEM from 390 CNTs, shows that the 80% of the CNTs measured present chiral angles in the range of 20°-30°. This high chiral angle predominance is independent of the choice of C precursor (butanol or toluene) or promoter (S or Se) used for the CVD growth of CNTs. The bias towards armchair SWNTs is thus intrinsic to the direct spinning process.

The chiral angle distribution matches theoretical predictions from atomistic modelling of SWNTs grown from molten catalyst.

Indeed, post-synthesis characterization of the catalysts suggests a liquid Fe-S shell in the catalyst particle, which according to our thermodynamics calculations would remain liquid at temperatures as low as 1000°C. During growth of the CNT, S in the liquid shell first assist in the stabilization of the edge of the nascent CNT, but later contributes to the rejection of the graphitic shell due to the high interfacial energy of the graphite basal plane and the Fe-C-S alloy.

It is fascinating that the molecular identity of the constituent CNTs in macroscopic A4 sheet CNT fiber samples (Fig. 1a), produced routinely in the laboratory and in larger quantities in semi-industrial settings, can be determined and precisely related to the CVD growth process conditions. Yet, it appears that most parameters adjusted over the last decade in the direct spinning process would have had little effect on chiral angle distributions and that the long term vision of single chirality continuous fibers will require different strategies to narrow the distribution without recourse to epitaxy or other mechanisms exclusive to solid catalysts. The results presented here thus call for more modelling work on CNT growth from liquid catalyst and on the different roles of promoters in high temperature CVD.

Acknowledgements

Notes and references

1   W. Lu, M. Zu, J.-H. Byun, B.-S. Kim and T.-W. Chou, *Adv. Mater.*, 2012, **24**, 1805–1833.
2   A. S. Wu and T.-W. Chou, *Mater. Today*, 2012, **15**, 302–310.
3   D. Eder, *Nanocarbon-inorganic hybrids: next generation composites for sustainable energy applications*, De Gruyter, Berlin ; Boston, Mass., 2014.
4   Z. Yang, J. Ren, Z. Zhang, X. Chen, G. Guan, L. Qiu, Y. Zhang and H. Peng, *Chem. Rev.*, 2015, **115**, 5159–5223.
5   J. J. Vilatela and R. Marcilla, *Chem. Mater.*, 2015.
6   M. W. Schauer and M. A. White, *MRS Proc.*, 2015, **1752**.
7   Y.-L. Li, I. A. Kinloch and A. H. Windle, *Science*, 2004, **304**, 276–278.
8   M. S. Motta, A. Moisala, I. A. Kinloch and A. H. Windle, *J. Nanosci. Nanotechnol.*, 2008, **8**, 2442–2449.
9   T. S. Gspann, F. R. Smail and A. H. Windle, *Faraday Discuss*, 2014.
10 D. N. Futaba, J. Goto, S. Yasuda, T. Yamada, M. Yumura and K. Hata, *Adv. Mater.*, 2009, **21**, 4811–4815.
11 R. M. Sundaram, K. K. K. Koziol and A. H. Windle, *Adv. Mater.*, 2011, **23**, 5064–5068.
12 Y. Liu, A. Dobrinsky and B. I. Yakobson, *Phys. Rev. Lett.*, 2010, **105**.
13 F. Ding, A. R. Harutyunyan and B. I. Yakobson, *Proc. Natl. Acad. Sci.*, 2009, **106**, 2506–2509.
14 V. I. Artyukhov, E. S. Penev and B. I. Yakobson, *Nat. Commun.*, 2014, **5**, 4892.
15 J. Kim, A. J. Page, S. Irle and K. Morokuma, *J. Am. Chem. Soc.*, 2012, **134**, 9311–9319.
16 S. Han, M. Yoon, S. Berber, N. Park, E. Osawa, J. Ihm and D. Tománek, *Phys. Rev. B*, 2004, **70**.
17 V. Jourdain and C. Bichara, *Carbon*, 2013, **58**, 2–39.
18 J. R. Sanchez-Valencia, T. Dienel, O. Gröning, I. Shorubalko, A. Mueller, M. Jansen, K. Amsharov, P. Ruffieux and R. Fasel, *Nature*, 2014, **512**, 61–64.
19 F. Yang, X. Wang, D. Zhang, J. Yang, D. Luo, Z. Xu, J. Wei, J.-Q. Wang, Z. Xu, F. Peng, X. Li, R. Li, Y. Li, M. Li, X. Bai, F. Ding and Y. Li, *Nature*, 2014, **510**, 522–524.
20 V. Reguero, B. Alemán, B. Mas and J. J. Vilatela, *Chem. Mater.*, 2014, **26**, 3550–3557.
21 M. S. Dresselhaus, G. Dresselhaus, A. Jorio, A. G. Souza Filho and R. Saito, *Carbon*, 2002, **40**, 2043–2061.
22 J. Wu, L. Xie, G. Hong, H. Lim, B. Thendie, Y. Miyata, H. Shinohara and H. Dai, *Nano Res.*, 2012, **5**, 388–394.
23 Z. Yu and L. E. Brus, *J. Phys. Chem. B*, 2001, **105**, 6831–6837.
24 R. Saito, M. Hofmann, G. Dresselhaus, A. Jorio and M. S. Dresselhaus, *Adv. Phys.*, 2011, **60**, 413–550.
25 M. S. Dresselhaus, G. Dresselhaus, R. Saito and A. Jorio, *Phys. Rep.*, 2005, **409**, 47–99.
26 S. D. M. Brown, A. Jorio, P. Corio, M. S. Dresselhaus, G. Dresselhaus, R. Saito and K. Kneipp, *Phys. Rev. B*, 2001, **63**, 155414.
27 F. Yang, X. Wang, D. Zhang, J. Yang, D. Luo, Z. Xu, J. Wei, J.-Q. Wang, Z. Xu, F. Peng, X. Li, R. Li, Y. Li, M. Li, X. Bai, F. Ding and Y. Li, *Nature*, 2014, **510**, 522–524.
28 G. A. Rance, D. H. Marsh, R. J. Nicholas and A. N. Khlobystov, *Chem. Phys. Lett.*, 2010, **493**, 19–23.
29 S. Chen, W. Yeoh, Q. Liu and G. Wang, *Carbon*, 2012, **50**, 4557–4565.
30 H. Kataura, Y. Kumazawa, Y. Maniwa, I. Umezu, S. Suzuki, Y. Ohtsuka and Y. Achiba, *Synth. Met.*, 1999, **103**, 2555–2558.
31 H. Liu, D. Nishide, T. Tanaka and H. Kataura, *Nat. Commun.*, 2011, **2**, 309.
32 S. M. Bachilo, M. S. Strano, C. Kittrell, R. H. Hauge, R. E. Smalley and R. B. Weisman, *Science*, 2002, **298**, 2361–2366.
33 P. Singh, S. Campidelli, S. Giordani, D. Bonifazi, A. Bianco and M. Prato, *Chem. Soc. Rev.*, 2009, **38**, 2214–2230.
34 J.-F. Colomer, L. Henrard, P. Lambin and G. V. Tendeloo, *Eur. Phys. J. B - Condens. Matter Complex Syst.*, 2002, **27**, 111–118.
35 V. I. Artyukhov, Y. Liu and B. I. Yakobson, *Proc. Natl. Acad. Sci.*, 2012, **109**, 15136–15140.
36 B. Mas, B. Alemán, I. Dopico, I. Martin-Bragado and J. J. Vilatela, **in preparation**.
37 T. Inoue, D. Hasegawa, S. Chiashi and S. Maruyama, *J Mater Chem A*, 2015, **3**, 15119–15123.
38 F. Ding, A. Rosén and K. Bolton, *Phys. Rev. B*, 2004, **70**.
39 F. Benissad, P. Gadelle, M. Coulon and L. Bonnetain, *Carbon*, 1988, **26**, 425–432.
40 C. Wu and V. Sahajwalla, *Metall. Mater. Trans. B*, 1998, **29**, 471–477.
41 S.-L. Chen, Y. Yang, S.-W. Chen, X.-G. Lu and Y. A. Chang, *J. Phase Equilibria Diffus.*, 2009, **30**, 429–434.
42 B. Delmon, *Catalyst Deactivation 1980 International Symposium Proceedings.*, Elsevier Science, Burlington, 1980.
43 D. Dilner, H. Mao and M. Selleby, *Calphad*, 2015, **48**, 95–105.